Global Environmental Science
www.sciltp.com/journals/ges

Article

Thermally Expanded Iron Phthalocyanine Nano-Crystal with Compressed Fe–N Bond Confined in Carbon Nitride for Fenton-like Reaction with Superior Activity and Stability

Jiaxin Li [1], Jiahao Cui [1,2,*], Kun Wang [1], Jiaran Yao [1], Di Meng [1], Wenying Yu [1], Qiang Huang [1] and Yubao Zhao [1,*]

[1] Center for Water Research, Institute of Environment and Health, Department of Chemistry and Environmental Science, Inner Mongolia Normal University, Hohhot 010010, China
[2] School of Municipal and Environmental Engineering, Henan University of Urban Construction, Pingdingshan 467036, China
* Correspondence: cuijh@huuc.edu.cn (J.C.); ybzhao@gzhu.edu.cn (Y.Z.)

How To Cite: Li, J.; Cui, J.; Wang K.; et al. Thermally Expanded Iron Phthalocyanine Nano-Crystal with Compressed Fe–N Bond Confined in Carbon Nitride for Fenton-like Reaction with Superior Activity and Stability. *Glob. Environ. Sci.* **2026**, *2*(4), 513–525. https://doi.org/10.53941/ges.2026.100030

Publication History

Received: 04 January 2026
Revised: 08 April 2026
Accepted: 15 May 2026
Published: 16 November 2026

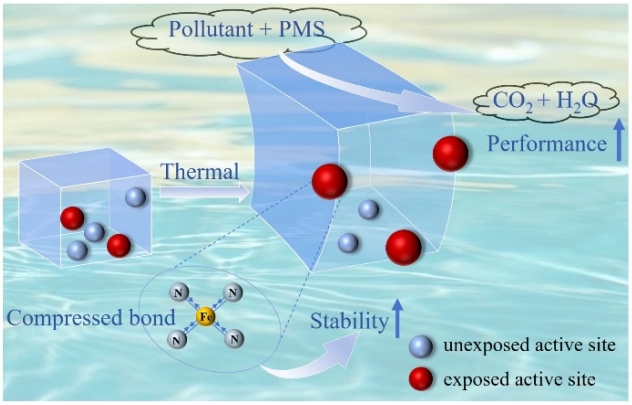
Keywords

peroxymonosulfate;
AOPs;
iron phthalocyanine;
high-valent iron-oxo species;
antibiotics;
stability

Highlights

- CN-confined FePc nanocrystals with compressed Fe–N bonds were constructed.
- FePc@CN-2 enabled rapid PMS activation for broad-spectrum antibiotic degradation.
- Fe^{IV}=O-dominated oxidation delivered high activity and over 2100 h flow stability.

Abstract: The persistence of emerging organic pollutants (EOPs) in the aquatic environment necessitates the development of selective and efficient treatment technologies. Peroxymonosulfate (PMS)-based advanced oxidation processes are promising, particularly when catalyzed by earth-abundant iron, which can generate high-valent Fe^{IV}=O, a selective oxidant with a long lifetime and high steady-state concentration. However, iron phthalocyanine (FePc), which mimics bioactive Fe–N_4 sites, suffers from limited active site exposure and low stability due to dense intermolecular packing. In this work, we address these challenges by thermally embedding FePc nanocrystals into a polymeric carbon nitride (CN) framework. This process expands the interlayer spacing and increases the dimension of the crystal cell, but compresses the Fe–N bonds, and thereby significantly enhances both catalytic activity and stability. The optimized catalyst of FePc@CN-2 could efficiently activate PMS and degrade a series of antibiotics. Specifically, for ofloxacin degradation, FePc@CN-2 exhibited a remarkable catalytic activity of more than 100 times greater than that of the control catalyst (FePc@CN-0). Furthermore, the composite demonstrated exceptional long-term stability in a continuous-flow system, operating for over 2100 h at a flow rate of 0.4 mL min^{-1} with >95% ciprofloxacin. Mechanistic studies substantiated that high-valent Fe^{IV}=O was the predominant reactive species. This work presents a unique structural-engineering strategy to unlock the potential of FePc catalysis, offering a robust and highly efficient catalyst for selective pollutant degradation.



Copyright: © 2026 by the authors. This is an open access article under the terms and conditions of the Creative Commons Attribution (CC BY) license (https://creativecommons.org/licenses/by/4.0/).
Publisher's Note: Scilight stays neutral with regard to jurisdictional claims in published maps and institutional affiliations.

1. Introduction

The pervasive presence of emerging organic pollutants (EOPs) in the global aquatic environment represents a significant ecological and public health concern [1–7]. Even at nanogram-per-litre concentration, long-term exposure to EOPs is hazardous, driving the need for innovative technologies towards the selective removal of EOPs [8]. Advanced Oxidation Processes (AOPs) are a series of efficient and eco-friendly treatment technologies widely applied in the removal of refractory organic contaminants from water and wastewater [9]. Mainstream AOPs include Fenton/Fenton-like oxidation, photocatalysis, ozonation, electrochemical oxidation, sulfate radical-based processes, and hybrid systems [10]. The core mechanism of AOPs lies in the in-situ generation of highly reactive oxygen species (ROS), mainly hydroxyl radicals (•OH), sulfate radicals ($SO_4^{\bullet-}$), superoxide anions ($O_2^{\bullet-}$), and singlet oxygen ($^1O_2$), which possess strong oxidation potential and can non-selectively attack organic pollutants, leading to efficient decomposition and even complete mineralization into CO_2, H_2O, and harmless inorganic ions. Compared with traditional physical separation and biological treatment, AOPs show remarkable advantages such as high oxidation efficiency, thorough mineralization capacity, broad applicability to various recalcitrant contaminants, mild reaction conditions, flexible operation, and low secondary pollution. Therefore, AOPs have become one of the most promising strategies for advanced water treatment and environmental remediation. Among these, sulfate radical-based AOPs have attracted significant interest for the degradation of refractory organic pollutants, exhibiting a higher oxidation potential, a wider pH applicability range (pH = 2–9), and a longer half-life (30–40 μs) [11–14]. PMS is a typical oxidizing agent characterized by its asymmetric structure, which can be activated through reactions with transition metal ions or oxides [15,16]. The catalytic mechanism of PMS involves both radical pathways, such as hydroxyl radicals (•OH) and sulfate radicals ($SO_4^{\bullet-}$), and non-radical pathways, including electron transfer-mediated reactions, high-valent metal species, and singlet oxygen [17]. Advanced oxidation processes utilizing PMS are highly promising, benefiting from the stability and safety of handling solid PMS salts [18–21]. Critically, the catalytic activation of PMS is governed by the nature of the active center and the support, enabling control over the generated reactive species and reaction mechanisms [22–25]. PMS can be activated through various methods, such as visible light irradiation, microwaves, and chemical catalysis [16]. Recently, single-atom catalysts (SACs) with atomically dispersed transition metals (such as Fe, Cu, Co, and Mn) anchored on nitrogen-doped carbon supports have garnered considerable interest in the field of PMS-based advanced Fenton-like reactions, due to the strong coordination effect of N and the excellent physicochemical properties [17]. From a sustainable perspective, iron stands out as the most suitable catalyst due to its earth abundance, low cost, and low environmental impact. In such systems, the high-valent Fe^{IV}=O species plays a crucial role. The combination of PMS with the mixed-valent Fe^{2+}/Fe^{3+} sites lead to the adsorption of the iron site onto the PMS molecule, forming an intermediate. Subsequently, the O–O bond undergoes heterolytic cleavage, generating the Fe^{IV}=O species [26]. Although its oxidation potential is milder than that of sulfate or hydroxyl radicals, Fe^{IV}=O possesses a substantially longer lifetime and can reach a higher steady-state concentration [27–29]. These properties render it exceptionally effective for the selective oxidation of target EOPs, as it is less susceptible to scavenging by the components of natural water matrix like mineral ions and natural organic matters (NOMs).

Within biological metabolism, enzymes containing heme or non-heme iron can produce high-valent Fe^{IV}=O, which acts as the active species for selective oxidation reactions [30]. Importantly, the electronic properties of the ligands and the microenvironment surrounding the iron are key determinants of its catalytic activity [31,32]. Iron phthalocyanine (FePc) possesses a unique Fe–N_4 structure similar to that in the bioactive molecules of heme and non-heme with an iron center. FePc thus exhibits remarkable potential in selective catalytic conversion reactions. However, two key challenges hinder the design of a robust FePc catalyst: (1) the limited exposure of active Fe–N_4 sites on the crystal surface, and (2) the weak van der Waals force between FePc molecules, which compromises its catalytic stability.

Herein, by thermal treatment of FePc and polymeric CN, FePc crystals were disassembled into nano-crystals and embedded in the CN framework. Most importantly, under such materials processing conditions, the crystal cell of FePc is expanded; meanwhile, the Fe–N_4 sites show a compressed Fe–N bond. All these structural features contribute to a significantly enhanced catalytic activity and stability in PMS activation for the degradation of a series of antibiotics. High-valent Fe^{IV}=O species was experimentally substantiated to be the predominant active species for antibiotic degradation.

2. Experimental Section

2.1. Synthesis of the Single Fe Atom Catalysts

CN was synthesized via the polymerization of the complex of melamine and cyanuric acid [33]. The single-atom Fe catalysts supported on CN were prepared through thermal polymerization of FePc and CN. Specifically, FePc and CN were mixed by ball-milling and then calcined in a tube furnace at 600 °C for 4 h under a nitrogen atmosphere, with a temperature ramping rate of 15 °C min^{-1}. The as-obtained samples were denoted as

 https://doi.org/10.53941/ges.2026.100030

FePc@CN-x, where x indicated the amount of CN used in the precursor.

2.2. Electron Paramagnetic Resonance (EPR) Experiments

5,5-Dimethyl-2-pyrrolidone-N-oxyl (DMPO) was used as a spin-trapping agent for detecting free radicals such as hydroxyl radical (•OH) and sulfate radical ($SO_4^{\bullet-}$). In a typical procedure, 0.22 mL of DMPO was dropped into 11 mL of a suspension containing 0.5 mM PMS. One millilitre aliquot was collected and analyzed by EPR to establish the baseline signal. Subsequently, 3 mg of catalyst was added to the vial to initiate the reaction. At specific time intervals, samples were withdrawn from the suspension, filtered, and then sealed in capillary tubes for EPR measurement. 2,2,6,6-tetramethylpiperidine (TEMP) was used as a spin-trapping agent for detecting singlet oxygen ($^1O_2$). A typical procedure involved preparing an 11 mL solution containing 0.5 mM PMS, 10 mM TEMP, and 22 ppm CIP in a glass vial, with continuous magnetic stirring. The reaction was initiated by adding 3 mg of the catalyst. At specified intervals, 1 mL of the suspension was collected, filtered, and then sealed in a capillary tube for EPR analysis.

2.3. Electrochemical Measurement

Electrochemical measurements were performed using a CHI-600 electrochemical workstation in a standard three-electrode configuration. The working electrode was prepared by coating a carbon paper with a catalyst ink, and the ink was prepared by ultrasonically dispersing 3 mg of catalyst in a solution of 300 μL isopropanol, 10 μL Nafion solution, and 100 μL deionized water. Following that, suspension (100 μL) was placed on 1 × 1 cm^2 carbon paper and allowed to dry naturally. A Pt wire and an Ag/AgCl electrode served as the counter and reference electrodes, respectively. All electrochemical measurements were conducted in a 500 mM Na_2SO_4 electrolyte solution without applying bias.

2.4. Batch and Flow Reaction Procedures

Batch reaction: the catalytic performance was evaluated in a batch reactor by adding 3 mg of the catalyst to 50 mL of a ciprofloxacin (CIP) solution (5 ppm). The degradation reaction was initiated by introducing PMS. Samples were collected at specified intervals and quenched with 20 μL of 1 M sodium thiosulfate to terminate the reaction before HPLC analysis.

Flow reactor: a fixed-bed flow reactor was constructed by packing a mixture of 30 mg of catalyst and silica sand into a silica tube (*Φ i.d.*= 1.2 cm). The residence time was 46 min, and the pressure drop was negligible. The reactant solution, containing 2 ppm CIP and 0.2 mM PMS, was fed into the reactor using a peristaltic pump at specified flow rates. Effluent was collected at specified intervals and quenched with an equal volume of 1 M sodium thiosulfate for subsequent HPLC analysis.

3. Results and Discussion

3.1. Physicochemical Properties of the Catalysts

By scanning electron microscopy (SEM) observation, the sample of FePc@CN-0 is an aggregation of irregular particles (Figure 1a,b). FePc@CN-2 presents a thin sheet-like structure, and the elements of C, N, O, and Fe are uniformly dispersed on the catalyst. (Figure 1c,d). X-ray photoelectron spectroscopy (XPS) was employed to investigate the chemical environments of the elements in FePc@CN-0 and FePc@CN-2. Elemental analysis by XPS survey scan (Figure S1) confirms the composition of the sample, which comprises C, N, O, and Fe. The C *1s* signal can be deconvoluted into three peaks at 284.8, 286.3, and 288.8 eV, which are, respectively, assigned to the carbon atoms in C=C, C–O and the C=N/O species (Figure 1e, Table S1) [34–37]. Further spectral deconvolution of the high-resolution N *1s* region (Figure 1f) reveals two distinct components at binding energies of 398.7 eV and 400.4 eV, which are characteristics of pyridinic N and pyrrolic N configurations, respectively [38–41]. There is redistribution of N species in the framework of the catalyst, and the proportion of the pyridinic N increase from 57.7% for FePc@CN-0 to 67.3% for FePc@CN-2 (Table S2), which might exhibit impact on the pollutant adsorption behavior and degradation process [42]. Introduction of CN in the precursor for sustaining the π-π interaction between the planar structure of FePc molecules increase the ratio of C/N, e.g., 1.4 and 1.8 respectively for FePc@CN-0 and FePc@CN-2 (Table S3).

The atomic dispersion of Fe atoms on the nitrogen-doped carbon and their coordination environment was further confirmed by aberration-corrected high-angle annular dark-field scanning transmission electron microscopy (AC-HAADF-STEM) and synchrotron X-ray absorption spectroscopy (XAS) [43]. The AC-HAADF-STEM image of FePc@CN-x exhibits bright spots indicative of atomically dispersed Fe within the CN matrix (Figure 2c). The distribution of N, C, and Fe in the catalyst is examined using energy-dispersive X-ray spectroscopy (EDS) mapping (Figure 1b,d), which shows a homogeneous dispersion of Fe across the CN matrix. The iron loadings in the samples were quantified by inductively coupled plasma optical emission spectroscopy (ICP-OES). As summarized in Table S4, the Fe content decreases with increasing CN amount, with Fe loadings of 5.1 wt.% for FePc@CN-2 and 4.5 wt.% for FePc@CN-0.

For further analyzing the status of the Fe species, high-angle annular dark-field scanning transmission electron microscopy (HAADF-STEM) was conducted. As shown in Figure 2c, there are no nanoparticles or clusters, and only bright spots are observed, demonstrating the atomic dispersion of the element

of Fe in FePc@CN-0 and FePc@CN-2. For understanding the local environment surrounding the Fe centers, synchrotron X-ray adsorption spectroscopy was performed. Figure 2d shows the extended X-ray absorption fine structure (EXAFS) spectra of the catalysts, along with reference samples including Fe_2O_3, iron (II) phthalocyanine (FePc), and Fe foil. As illustrated in the inset of Figure 2d, the absorption edge energy of FePc@CN-0 and FePc@CN-2 lies between FePc and Fe_2O_3. By using the edge energy of the reference samples Fe, FePc, and Fe_2O_3 with valences of 0, +2, and +3, respectively. The valence of Fe on the single-atom catalyst is determined to be +2.49 for FePc@CN-0 and +2.51 for FePc@CN-2 (Figure 2e).

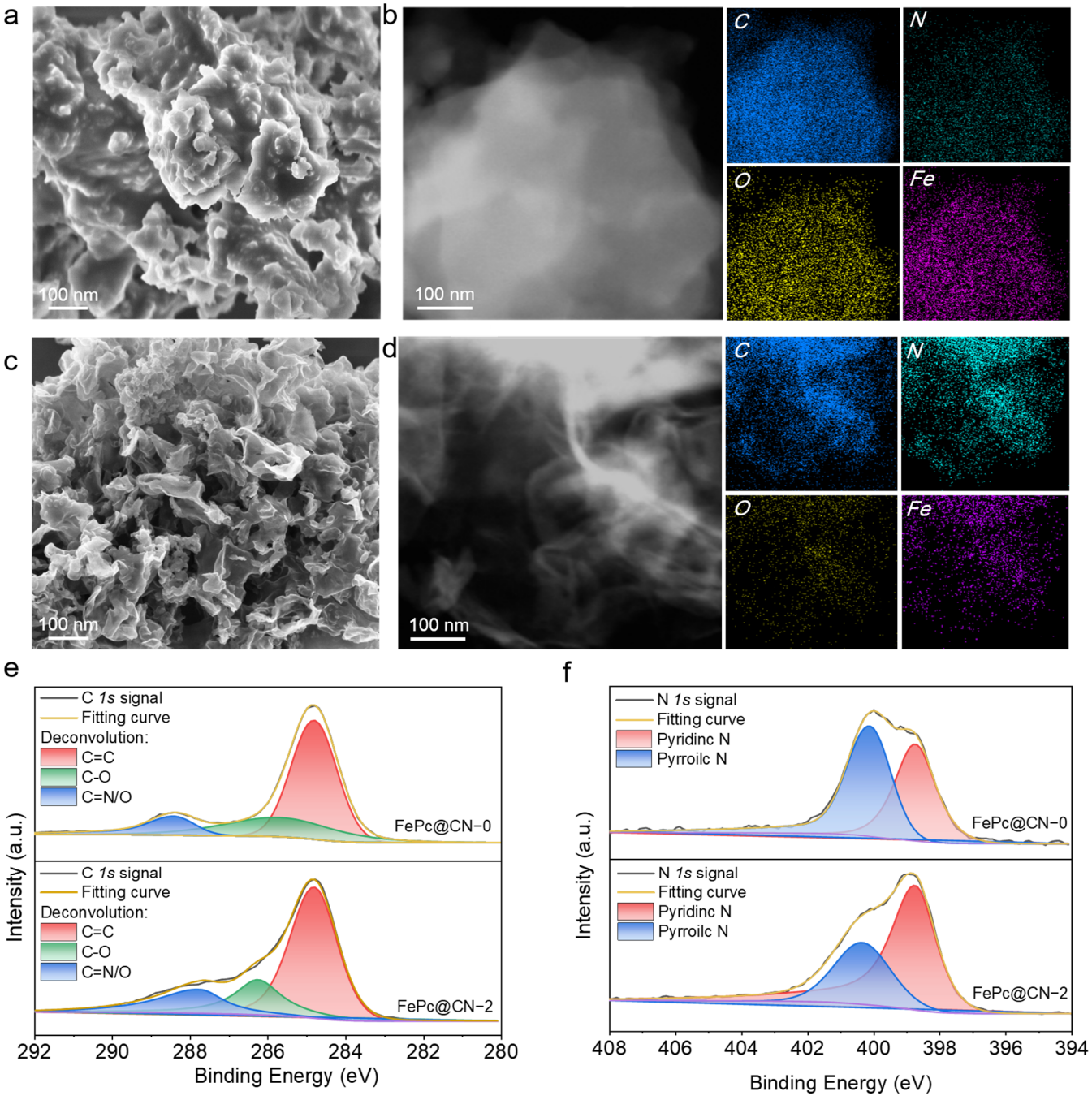


Figure 1. Scanning electron microscopy (SEM) images (**a**,**c**), Scanning Transmission Electron Microscopy (STEM) and Energy-dispersive X-ray spectroscopy (EDS) mapping (**b**,**d**) of FePc@CN-0 (**a**,**b**) and FePc@CN-2 (**c**,**d**). X-ray photoelectron spectroscopy (XPS) profiles and the deconvoluted peaks of C *1s* (**e**) and N *1s* (**f**) signals.

 https://doi.org/10.53941/ges.2026.100030

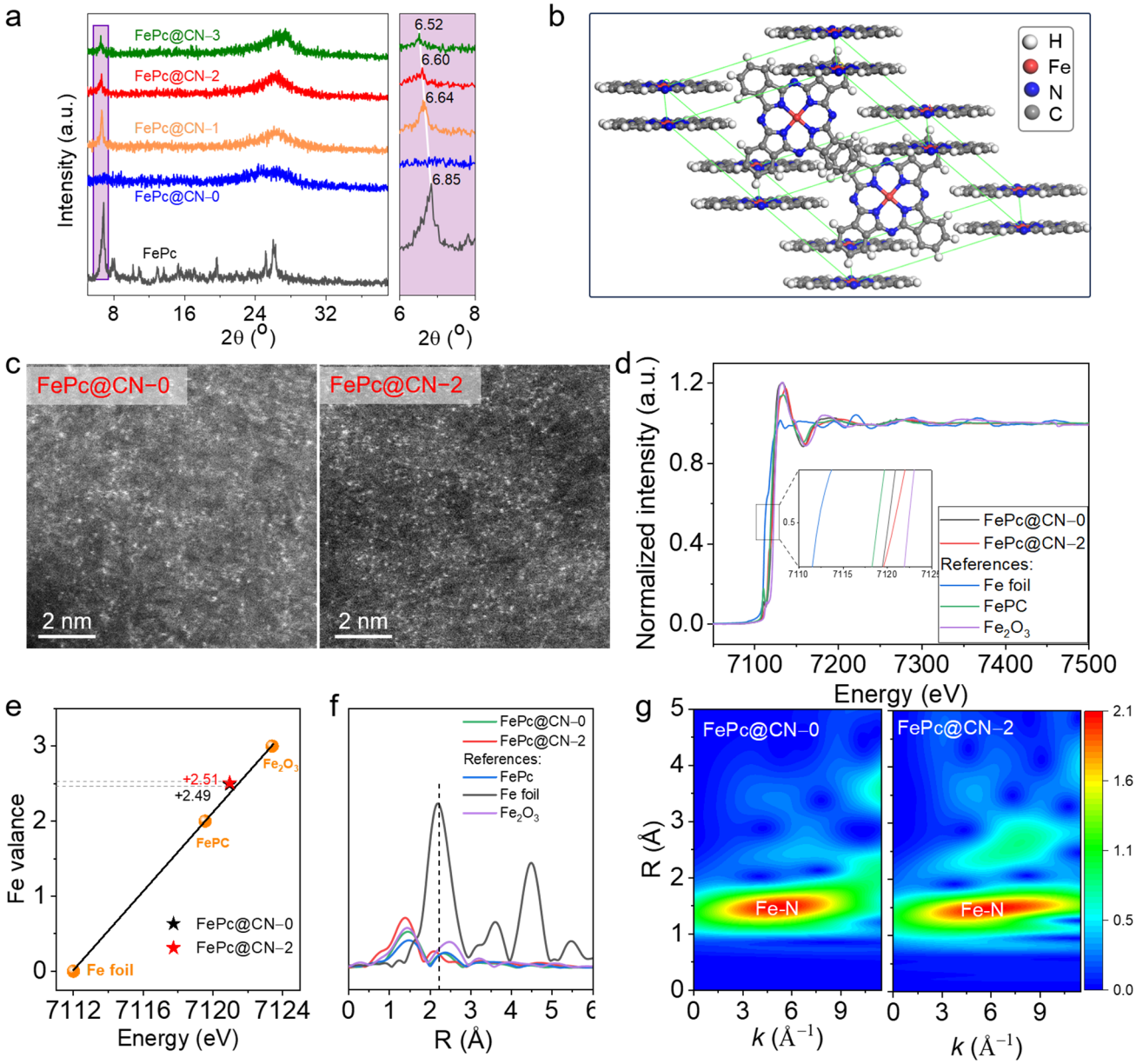


Figure 2. (**a**) X-ray diffraction profiles. (**b**) Atomic arrangement of iron phthalocyanine (FePc) layer stacking structure. (**c**) Aberration-corrected atomic resolution HAADF-STEM micrographs. (**d**) Fe *K*-edge EXAFS spectra of the single-atom catalysts with reference samples; the inset is the zoomed-in area marked by a rectangle. (**e**) Valence of the Fe element in single-atom catalysts and reference samples determined by the edge energy of X-ray adsorption spectra. (**f**) k^2-weighted EXAFS spectra in *R* space; *R* is the interatomic distance, indicating the radial distance without phase correction. (**g**) Wavelet transforms of k^2-weighted EXAFS spectra of FePc@CN-0 and FePc@CN-2.By XRD characterization, FePc shows a standard diffraction pattern with a predominant peak at 6.85°, which is assigned to the diffraction from (100) planes (Figure 2a,b) [44]. Thermal treatment of FePc affords FePc@CN-0, and the XRD pattern states that the repeating arrangement of the FePc molecules vanished during the thermal treatment. While for the samples synthesized from pyrolysis of FePc in the presence of CN framework, ordered arrangement of FePc is sustained; and most importantly, the arrangement of the FePc molecules changes, demonstrated by the shifting of the (100) diffraction peaks to a lower angle with increasing proportion of CN in the precursor (Figure 2a, inset). In the presence of the CN framework, FePc crystals survive during the thermal processing, and most importantly, the size of the crystal cell changes, which might result in the variation in the local chemical environment of the Fe center as well as its catalytic performance. Moreover, the broad peak observed at 25.9° corresponds to the layer-stacking structure CN. No diffraction peaks associated with crystalline Fe species are detected, suggesting the absence of Fe nanoparticles in the catalysts (Figure 2a).

The Fourier transform of the EXAFS spectrum for the Fe foil reveals a first-shell Fe–Fe scattering path at 2.12 Å (Figure 2f). In the reference sample of FePc, the first-shell Fe–N scattering path appears at 1.50 Å [42,45–47]. The thermal treatment poses a negligible impact on the length of Fe–N, and the Fe–N scattering path in FePc@CN-0 is

1.47 Å. In contrast, the scattering path of Fe–N in FePc@CN-2 is 1.39 Å, which is much shorter than that of FePc@CN-0. Fitting the EXAFS profile reveals the coordination number and the bond length of the central Fe atoms with respect to neighbouring atoms. The first shell Fe–N coordination number is determined to be ~4, and the bond distance is ~2.19 Å for FePc@CN-0; while for FePc@CN-2, the coordination number of the Fe center is 4, and the bond length of Fe–N is 1.92 (Figure S2 and Table S5). The peak at 1.39 Å represents the raw scattering path distance. After correction during the fitting process, the refined Fe–N bond length is determined to be approximately 1.92 Å. Short Fe–N bond speaks for a strong bond energy, which might contribute positively to a robust active center in the PMS activation for organic pollutant degradation [48]. The wavelet transform (WT) spectrum of the FePc@CN-0 and FePc@CN-2 present contour intensity maxima at a *k*-value of 5.8 $Å^{-1}$ and 6.2 $Å^{-1}$, respectively, corresponding to the Fe–N coordination, and there is no Fe–Fe signal, which once again supports the atomic dispersion of the Fe center (Figure 2g) [49–52].

3.2. Catalytic Performance Evaluation

Ciprofloxacin (CIP), an antibiotic widely used and frequently detected in aquatic environments, has been identified as one of the emerging organic pollutants (EOPs) that raise public concern [54,55]. CIP is therefore selected as a model pollutant to assess the performance of the catalysts. As shown in Figure 3a, the catalytic activity varies with the amount of CN in the catalysts. For the FePc@CN-0 catalyzed reaction system, CIP removal is around 20% at the reaction time of 10 min. In contrast, FePc@CN-2 exhibits the optimum catalytic performance, and complete removal of 5 ppm CIP is achieved within 10 min under mild reaction conditions of 0.06 g L^{-1} of FePc@CN-2 and 0.5 mM of PMS (Figure 3a). The pseudo-first order reaction rate constant in the FePc@CN-2 catalyzed reaction system is 0.500 min^{-1}, which is 29 time that of the FePc@CN-0 catalyzed reaction system (Figure S3). Moreover, norfloxacin (NOX) and ofloxacin (OFX), like ciprofloxacin, are all quinolone antibiotics; as compared with FePc@CN-0, the catalytic performance of FePc@CN-2 is remarkably superior in the degradation of NOX and OFX. The reaction rate constant in the NOX degradation reaction is 0.016 min^{-1} by FePc@CN-0 catalysis, while this value ramps to 0.500 min^{-1} in the FePc@CN-2 catalyzed reaction system. In the degradation of OFX, the reaction rate constant for the FePc@CN-2 catalyzed reaction system reaches a remarkable value of 4.810 min^{-1}, which is 104 times that of the case with FePc@CN-0 catalysis (Figure 3b,c). FePc@CN-2 is then applied in the degradation of various antibiotics in the presence of PMS. As shown in Figure 3e, twelve different types of antibiotics can be efficiently removed within 20 min, demonstrating the good general applicability of FePc@CN-2 catalyzed PMS activation for antibiotics removal from water. Additionally, we compared the activation effects of representative single-atom catalysts on PMS from recent literature and found that our designed catalyst ranks among the top in key performance metrics (Table S7).

The stability of the catalysts in pollutant degradation was tested in a fixed-bed flow reactor (Figure S4). As displayed in Figure 3f, FePc@CN-0 demonstrates low activity and stability, with the CIP removal efficiency declining rapidly after 194 h on stream. In contrast, FePc@CN-2 demonstrates markedly enhanced stability, sustaining nearly complete pollutant removal over 660 h at a flow rate of 1.6 mL min^{-1}. The performance equates to a treatment capacity of 2112 L of 2 ppm CIP solution per gram of catalyst. Moreover, at a reduced flow rate of 0.4 mL min^{-1}, FePc@CN-2 achieves near-complete pollutant elimination for up to 2100 h, with high CIP removal of >95%. The concentration of the leached metal ions in the effluent is below 0.004 ppm, which is not hazardous to the aquatic environment. The crystal structure can remain unchanged, demonstrating its sufficient stability (Figure S5). Additionally, a pronounced decrease in catalytic performance was observed at a flow rate of 1.6 mL min^{-1}. This can be attributed to the insufficient residence time of PMS on the catalyst surface, leading to inadequate PMS activation. As a result, CIP degradation proceeds incompletely, generating aromatic intermediates, piperazine, and other byproducts. These species adsorb onto the catalyst surface via π–π stacking interactions, occupying active sites and inducing rapid catalytic deactivation. The sustained high-efficiency degradation and low iron ion leaching rate observed in the fixed-bed flow reactor demonstrate the stability of FePc@CN-2 under flow reaction conditions. During the preparation of FePc@CN-2, the anisotropic thermal expansion of the CN support and FePc molecules triggers interfacial and interlayer expansion upon heating. Owing to the mechanical stress generated at their interface, this expansion compresses the Fe–N bonds within FePc molecules, thereby significantly enhancing the stability of the Fe–N active sites. This provides promising prospects for its application in potential water treatment operations.

Considering the potential application in natural water with ions and natural organic matter (NOMs), the impact of the mineral ions and NOMs on the catalytic performance of FePc@CN-2 in antibiotics degradation is examined. As shown in Figure S6, chloride, dihydrogen phosphate, sulfate, and nitrate ions exhibit negligible impact on the pollutant degradation. The influence of natural organic matters (NOMs) on pollutant degradation is further investigated in the presence of humic acid, and CIP could be removed efficiently in the presence of 5 ppm of humic acid. Additionally, the effect of the initial pH of

 https://doi.org/10.53941/ges.2026.100030

the solution on degradation efficiency is examined. As shown in Figure S7, CIP is efficiently eliminated within 10 min across a broad pH range from 3.0 to 11.0. Moreover, tap water and water from the Zhujiang River are also tested to evaluate the adaptability of the catalytic reaction system (detailed water quality data see Table S6). As shown in Figure S8, CIP is removed within 20 min in the FePc@CN-2 catalyzed system in both tap water and river water. These results suggest the potential applicability of this reaction system in real water matrices.

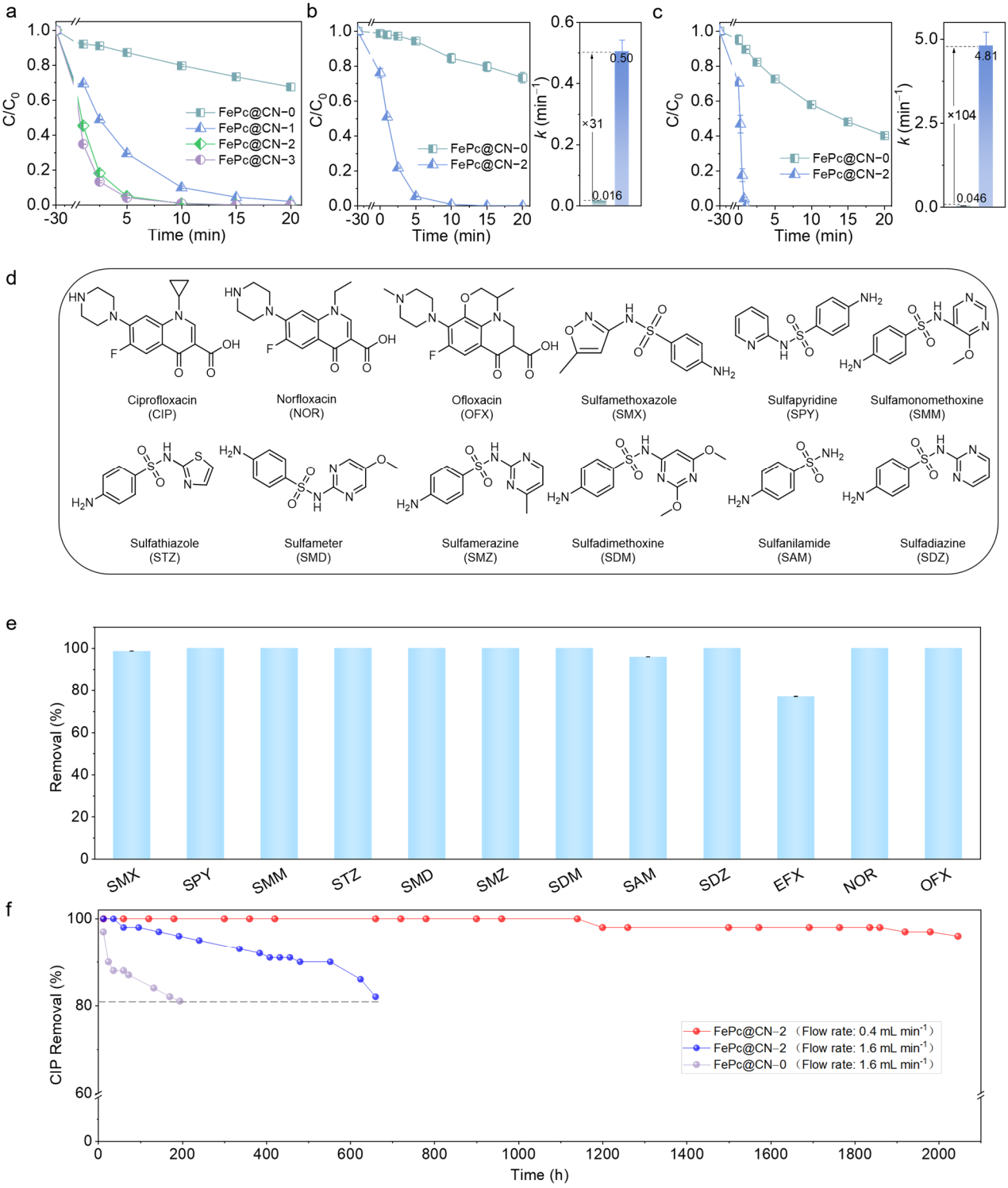


Figure 3. (**a**) Catalytic performance of FePc@CN-x in CIP degradation in the presence of PMS. (**b**,**c**) FePc@CN-0 and FePc@CN-2 catalyzed degradation of norfloxacin (**b**) and ofloxacin (**c**). (**d**) Molecular structure of a series of antibiotics. (**e**) The catalytic performance of FePc@CN-2 in the degradation of various organic pollutants in the presence of PMS at 20 min. Reaction conditions: [pollutant] = 5 mg L^{-1}, [PMS] = 0.5 mM, [catalyst] = 0.06 g L^{-1}. (f) Catalytic performance of FePc@CN-0 and FePc@CN-2 in a fixed-bed flow reactor. Reaction conditions: [catalyst loading] = 30 mg, [pollutant] = 2 mg L^{-1}, [PMS] = 0.2 mM.

3.3. Mechanistic Insights into PMS Activation over the Single-Atom Fe Catalyst

A mechanistic study was subsequently carried out to elucidate the origin of the high catalytic efficiency observed over the single-atom Fe catalyst. First, the roles of radical species, namely hydroxyl radical ($^{\bullet}OH$) and sulfate radical ($SO_4^{\bullet-}$), in the degradation of CIP were evaluated through radical quenching experiments and EPR spectroscopy. Due to high reaction rate constants, e.g., k ($^{\bullet}OH/CH_3OH$) = (1.2–2.8) × 10^9 M^{-1} s^{-1}, k ($SO_4^{\bullet-}/CH_3OH$) = (1.6–7.8) × 10^7 M^{-1} s^{-1}, and k ($^{\bullet}OH$/TBA) = (3.8–7.6) × 10^8 M^{-1} s^{-1}, methanol and tert-butyl alcohol (TBA) are sensitive probe molecules for those radicals [55,56]. To assess the contribution of free radicals to CIP degradation, quenching experiments were conducted using the probing molecules of methanol and TBA. Figure 4a shows that the degradation proceeded rapidly despite the presence of 500 mM methanol, a concentration 3.2 × 10^3 times higher than that of CIP. When TBA was used as the radical quencher, similar experimental results were presented, indicating that the contribution of radicals to CIP degradation is negligible.

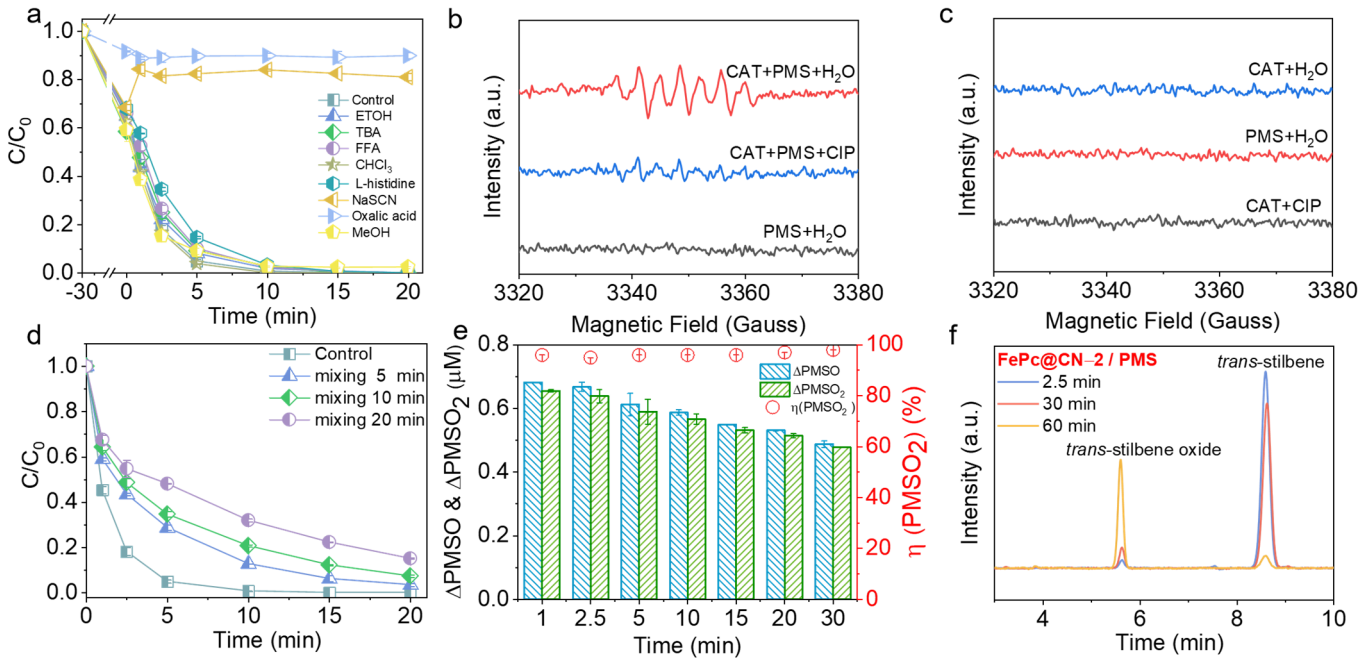


Figure 4. (**a**) Impact of the quenching agents on CIP degradation in FePc@CN-2 catalyzed reaction. (**b**) Probing the active species in the reaction system by electron spin resonance (EPR) spectroscopy with DMPO as the spin-trapping agent. (**c**) Identifying the possible contribution of the singlet oxygen in the reaction system by EPR with TEMP as the spin-trapping agent. (**d**) CIP removal in the reaction system of premixed PMS and FePc@CN-2 for a specified reaction time. (**e**) Selective oxidation of methyl phenyl sulfoxide (MPSO) to methyl phenyl sulfone ($MPSO_2$) by high-valent Fe (Fe^{IV}=O). (**f**) Selective oxidation of trans-stilbene by FePc@CN-2 catalyzed PMS activation. Reaction conditions: [CIP] = 5 mg L^{-1}, [PMS] = 0.5 mM, [catalyst] = 0.06 g L^{-1}, [EtOH] = 500 mM, [MeOH] = 500 mM, [TBA] = 500 mM, [FFA] = 0.3 mM, [$CHCl_3$] = 0.3 mM, [NaSCN] = 3 mM, [Oxalic acid] = 3 mM, [BYX] = 0.1 mM, [L-histidine] = 0.3 mM, [MPSO] = 0.5 mM.

The lack of significant inhibition on CIP degradation upon addition of chloroform ($CHCl_3$, $O_2^{\bullet-}$ scavenger) ruled out the contribution of $O_2^{\bullet-}$ in the reaction process [58]. The potential role of singlet oxygen ($^1O_2$) was thereafter investigated. Furfuryl alcohol and L-histidine, which usually act as trapping agents for $^1O_2$ with a high reaction rate constant [59,60], were introduced into the system. As shown in Figure 4a, the addition of 0.3 mM furfuryl alcohol in the reaction system does not impose any noticeable influence on the degradation of CIP, and the presence of 0.3 mM L-histidine also poses no impact on CIP degradation. Moreover, no characteristic triplet signals indicative of 2,2,6,6-tetramethylpiperidine-N-oxide (TEMPO) formation are detected by EPR spectroscopy (Figure 4c). Hence, the involvement of singlet oxygen in the CIP degradation process is excluded.

Electrochemical measurements were then conducted to further analyze the reaction process. As evidenced by the *I*–*t* curve (Figure S9), the system exhibits a current enhancement upon the spike of PMS and CIP; and the electrochemical reaction system with a working electrode loaded with the active material of FePc@CN-2 shows a stronger current response than that with FePc@CN-0, demonstrating the interface-mediated reaction process rather than a radical-dominated bulk reaction. Further experimental investigations employing premixing of the catalyst and PMS before contacting the pollutant were conducted. As shown in Figure 4d, CIP degradation performance negatively relates to the duration

 https://doi.org/10.53941/ges.2026.100030

of mixing FePc@CN-2 and PMS before CIP addition in the mixture. These data exclude the possible contribution of the mediated-electron transfer pathway [60].

Based on the experimental evidence, the commonly implicated radicals, singlet oxygen, and mediated-electron transfer pathways can be excluded as the predominant contributors. In iron-based homogeneous or heterogeneous AOP, high-valence iron-oxo species (Fe^{IV}=O) have been reported to be a crucial intermediate. [61] To this end, we investigated whether Fe^{IV}=O acts as a mediator in this system, employing electron paramagnetic resonance (EPR) spectroscopy with 5,5-dimethyl-1-pyrrolidone N-oxide (DMPO) as the spin trap for verification. As shown in Figure 4b, the signals detected after introducing PMS and DMPO in the absence of a catalyst were too weak to be identified. With the addition of FePc@CN-2, the characteristic quintet signals of DMPOX (5,5-dimethyl-2-pyrrolidone-N-oxide) started to emerge; no characteristic signals corresponding to hydroxyl or sulfate radicals were observed in the spectrum. Since DMPOX is known to form mainly through the direct oxidation of DMPO without the involvement of radical species [62,63], it is reasonable to propose that DMPOX generation was initiated by Fe^{IV}=O oxidation. Furthermore, the addition of CIP leads to a decrease in the intensity of the heptet signal. This suggests that the Fe^{IV}=O species is involved in both the DMPO oxidation and the CIP degradation process (Figure 4b). It is, accordingly, plausible to propose that the high-valent Fe^{IV}=O species can be predominant in the reaction system. SCN^- and oxalate ions are able to coordinate with the Fe center, and act as quenchers to evaluate the involvement of high-valent Fe^{IV}=O species [64–67]. As shown in Figure 4a, the addition of 3 mM NaSCN significantly inhibited CIP degradation, indicating that high-valent iron species (Fe^{IV}=O) are likely the key factor driving CIP degradation. In the presence of 3 mM oxalate, CIP degradation was obviously inhibited, indicating that PMS activation primarily occurs at the Fe center within FePc@CN-2. Additionally, the high-valent Fe^{IV}=O species are able to selectively transform methyl phenyl sulfoxide (MPSO) into methyl phenyl sulfone ($MPSO_2$) through an oxygen atom transfer process [35,37,68]. The selective oxidation of MPSO to $MPSO_2$ was thus utilized as a probe reaction to detect high-valent iron-oxo species (Figure S10) [69]. As shown in Figure 4e, FePc@CN-2 demonstrated remarkable catalytic performance in the selective conversion of MPSO to $MPSO_2$, with a high selectivity ranging from 95% to 98%, indicating the generation of Fe^{IV}=O species in the reaction system. To further confirm the role of high-valent Fe^{IV}=O, the transformation of trans-stilbene into trans-stilbene oxide, a typical oxygen atom transfer reaction, was employed as a probe reaction [70]. In the FePc@CN-2 catalyzed reaction, the peak of trans-stilbene decreased, and the signal of stilbene oxide increased simultaneously (Figure 4f); while in the case with FePc@CN-0 as the catalyst, the formation of stilbene-oxide was also detected, but with a much lower catalytic activity as compared with FePc@CN-2. This is consistent with the distinction between FePc@CN-2 and FePc@CN-0 in catalytic degradation of antibiotics, strongly demonstrating that the high-valent Fe^{IV}=O is the predominant active species [40].

Based on Fe^{IV}=O, we summarized the degradation mechanism on FePc@CN-2. Upon addition of PMS, the mixed-valent Fe^{2+}/Fe^{3+} sites undergo initial electron transfer with PMS, promoting O-O bond cleavage and forming an Fe^{3+}–O–OSO_3^- peroxy intermediate [29]. Subsequently, this intermediate undergoes a second internal electron transfer, with Fe^{3+} transferring another electron to the O-O bond, thereby promoting its complete cleavage. With the complete heterolytic cleavage of the O–O bond in the peroxy intermediate, an electron rearrangement occurs, yielding the highly oxidized Fe^{IV}=O species, which becomes the primary active species in CIP degradation. Subsequently, Fe^{IV}=O attacks electron-rich groups such as the piperazine ring of CIP via an oxygen atom transfer (OAT) pathway, completing the degradation.

4. Conclusions

By thermal treatment of FePc and CN, an FePc crystal with an expanded crystal cell and compressed Fe–N bond is embedded in CN, forming an efficient and stable catalyst for PMS activation and antibiotics degradation. Using the optimum catalyst of FePc@CN-2 to activate PMS, a series of antibiotics could be efficiently removed. In the degradation of OFX, the catalytic performance of FePc@CN-2 exceeded that of FePc@CN-0 by a remarkably high factor of over 104. Meanwhile, FePc@CN-2 exhibited superior stability in a flow reactor, and the catalyst could run 2100 h on stream with a flow rate of 0.4 mL min^{-1}. Further increase the flow rate to 1.6 mL min^{-1}, the flow reactor could run for 660 h with CIP removal of >80%, corresponding to a water treatment capacity of 2112 L per gram catalyst. Mechanistic investigations involving quenching experiments and spectroscopy investigations substantiated that the high-valent iron-oxo species were the predominant active species for antibiotic degradation. The findings in this work demonstrate a unique approach for improving the catalytic activity and stability of FePc, and shed light on the design of robust FePc catalysts for various applications.

Supplementary Materials

The additional data and information can be downloaded at: https://media.sciltp.com/articles/others/2611161340505137/GES-26010010-SI.pdf. Experimental details, EXASF data analysis, XPS data analysis, Supporting Figures and Tables. References [71–78] are cited in Supplementary Materials.

Author Contributions

J.L.: data curation, software, visualization, writing—original draft preparation; J.C.: conceptualization, methodology; K.W.: investigation; J.Y.: investigation; D.M.: investigation; W.Y.: investigation; Q.H.: investigation; Y.Z.: conceptualization, supervision, writing—reviewing and editing. All authors have read and agreed to the published version of the manuscript.

Funding

This research was funded by National Natural Science Foundation of China (22476101, 21976041), Program for Young Talents of Science and Technology in Universities of Inner Mongolia Autonomous Region (NJYT25013).

Institutional Review Board Statement

Not applicable.

Informed Consent Statement

Not applicable.

Data Availability Statement

The raw experimental data, characterization spectra and degradation kinetic datasets generated in this study are available from the corresponding author upon reasonable request.

Acknowledgment

The beamline scientists on BL11B and BL08U1A at Shanghai Synchrotron Radiation Facility (SSRF) are acknowledged.

Conflicts of Interest

The authors declare no conflict of interest.

Use of AI and AI-Assisted Technologies

No AI tools were utilized for this paper.

References

1. Shen, Y.; Yang, M.; Zhu, C.; et al. Enhanced selectivity in PMS activation via non-metal doping for efficient $^1O_2$ generation in emerging organic pollutants degradation. *ACS EST Engg.* **2024**, *4*, 2839–2851.
2. Wang, S.; Xu, L.; Wang, J. Iron-based dual active site-mediated peroxymonosulfate activation for the degradation of emerging organic pollutants. *Environ. Sci. Technol.* **2021**, *55*, 15412–15422.
3. Zheng, J.; Lin, Q.; Wu, Y.; et al. Key coordination of oxygen doping in Fe single-atoms enhances nonradical activation of peroxymonosulfate: The formation of high-valent Fe species and electron transfer. *Chem. Eng. J.* **2024**, *489*, 151307.
4. Xu, J.; Yao, Y.; Zhu, C.; et al. Unveiling enhanced electron-mediated peroxymonosulfate activation for degradation of emerging organic pollutants. *Appl. Catal. B* **2024**, *341*, 123356.
5. Li, M.; Chen, J.; Wu, W.; et al. Diatomic Fe-Fe catalyst enhances the ability to degrade organic contaminants by nonradical peroxymonosulfate activation system. *Nano Res.* **2023**, *16*, 4678–4684.
6. An, S.; Zhang, G.; Wang, T.; et al. High-density ultra-small clusters and single-atom Fe sites embedded in graphitic Carbon nitride (g-C_3N_4) for highly efficient catalytic advanced oxidation processes. *ACS Nano.* **2018**, *12*, 9441–9450.
7. Zhang, B.; Li, X.; Akiyama, K.; et al. Elucidating the mechanistic origin of aspin state-dependent FeN_x–C catalyst toward organic contaminant oxidation via peroxymonosulfate activation. *Environ. Sci. Technol.* **2021**, *56*, 1321–1330.
8. Lee, Y.-Y.; Fan, C.; Haque, F. Hybrid combination of advanced oxidation and biological processes for the micropollutant removal of carbamazepine. *NPJ Clean Water* **2022**, *5*, 60.
9. Li, F.; Liu, K.; Bao, Y.; et al. Molecular level removal of antibiotic resistant bacteria and genes: A review of interfacial chemical in advanced oxidation processes. *Water Res.* **2024**, *254*, 121373.
10. Liu, J.; Wu, H.; Sun, J.; et al. Non-TiO_2-based photoanodes for photoelectrocatalytic wastewater treatment: electrode synthesis, evaluation, and characterization. *EES Catal.* **2025**, *3*, 921–942.
11. Xiao, Y.; He, J.; An, J.; et al. Highly efficient activation of peroxymonosulfate by ZIF-67 anchored cotton derived for ciprofloxacin degradation. *Environ. Res.* **2024**, *244*, 117863.
12. Yang, L.; Yang, H.; Yin, S.; et al. Fe Single-Atom Catalyst for Efficient and Rapid Fenton-Like Degradation of Organics and Disinfection against Bacteria. *Small* **2022**, *18*, 202104941.
13. Liu, Y.; Zhou, H.; Jin, C.; et al. Bio-porphyrin supported single-atom iron catalyst boosting peroxymonosulfate activation for pollutants degradation: A Singlet Oxygen-dominated nonradical pathway. *Appl. Catal. B* **2023**, *338*, 123061.
14. Li, T.; Wang, X.; Fan, Z.; et al. Unique role of doped Mo into Fe-based catalyst to intensify peroxydisulfate activation for micropollutants degradation: Promote the conversion of $SO4^{\bullet-}$ to Fe^{IV}=O. *Chem. Eng. J.* **2024**, *500*, 157255.
15. Zheng, X.; Niu, X.; Zhang, D.; et al. Metal-based catalysts for persulfate and peroxymonosulfate activation in heterogeneous ways: A review. *Chem. Eng. J.* **2022**, *429*, 132323.
16. Li, D.; Zhang, S.; Li, S.; et al. Mechanism of the application of single-atom catalyst-activated PMS/PDS to the degradation of organic pollutants in water environment: A review. *J. Clean. Prod.* **2023**, *397*, 136468.
17. Luo, C.; Zhang, S.; Chen, Y.; et al. The cascading anchoring strategy fabrication of high-coordination single-atom catalyst: Efficient peroxymonosulfate activation with high $^1O_2$ selectivity. *J. Hazard. Mater.* **2025**, *498*, 140012.
18. Wu, Q.-Y.; Yang, Z.-W.; Wang, Z.-W.; et al. Oxygen doping of cobalt-single-atom coordination enhances peroxymonosulfate activation and high-valent cobalt–oxo

species formation. *Proc. Natl. Acad. Sci. USA* **2023**, *120*, e2219923120.
19. Jin, C.; Han, B.; Luo, C.; et al. Precise synthesis of Fe single-atom catalysts on montmorillonite/g-C_3N_4 heterostructures for highly efficient fenton-like degradation of organic pollutants. *Water Res.* **2025**, *287*, 124420.
20. Zheng, J.; Lin, Q.; Liu, Y.; et al. Efficient activation of peroxymonosulfate by Fe single-atom: The key role of Fe-pyrrolic nitrogen coordination in generating singlet oxygen and high-valent Fe species. *J. Hazard. Mater.* **2024**, *462*, 132753.
21. Shao, S.; Cui, J.; Wang, K.; et al. Efficient and durable single-atom Fe catalyst for Fenton-like reaction via mediated Electron-Transfer mechanism. *ACS EST Engg.* **2022**, *3*, 36–44.
22. Lan, M.-Y.; Li, Y.-H.; Wang, C.-C.; et al. Multi-channel electron transfer induced by polyvanadate in metal-organic framework for boosted peroxymonosulfate activation. *Nat. Commun*. **2024**, *15*, 7208.
23. Jin, S.; Tan, W.; Huang, Y.; et al. Remote tuning of single-atom Fe-N5 sites via high-coordination defects for enhanced Fenton-like water decontamination. *Nat. Commun.* **2025**, *16*, 10455.
24. Dai, H.; Zhao, Z.; Wang, K.; et al. Regulating electronic structure of Fe single-atom site by S/N dual-coordination for efficient Fenton-like catalysis. *J. Hazard. Mater.* **2024**, *465*, 133399.
25. Miao, J.; Zhu, Y.; Lang, J.; et al. Spin-state-dependent peroxymonosulfate activation of aingle-atom M–N moieties via a radical-free pathway. *ACS Catal.* **2021**, *11*, 9569–9577.
26. Ding, Y.; Cui, K.; Liu, X.; et al. Axial g-C3N4 coordinated iron(III) phthalocyanine mediated ultra-efficient peroxymonosulfate activation for high-valent iron species generation. *Appl. Catal. A* **2022**, *641*, 118679.
27. Zhao, Z.; Dai, H.; Nie, T.; et al. Dynamic electronic modulation of single-atom Fe sites with p-block metal coordination enables highly selective generation of FeIV = O in Fenton-like reactions. *Nat. Commun.* **2025**, *16*, 11290.
28. Yin, Y.; Li, W.; Li, X.; et al. Single-atom Fe-N_4 sites on crumpled N-C-MoS_2 nanospheres for peroxymonosulfate activation and Fe^{IV}=O generation. *Chem. Eng. J.* **2025**, *520*, 165664.
29. Qian, K.; Chen, H.; Li, W.; et al. Single-Atom Fe Catalyst Outperforms Its Homogeneous Counterpart for Activating Peroxymonosulfate to Achieve Effective Degradation of Organic Contaminants. *Environ. Sci. Technol*. **2021**, *55*, 7034–7043.
30. Nam, W. High-Valent Iron(IV)–Oxo Complexes of Heme and Non-Heme Ligands in Oxygenation Reactions. *Acc. Chem. Res.* **2007**, *40*, 522–531.
31. Kwong, K.W.; Patel, D.; Malone, J.; et al. An investigation of ligand effects on the visible light-induced formation of porphyrin–iron(IV)-oxo intermediates. *New J. Chem*. **2017**, *41*, 14334–14341.
32. Hohenberger, J.; Ray, K.; Meyer, K. The biology and chemistry of high-valent iron–oxo and iron–nitrido complexes. *Nat. Commun*. **2012**, *3*, 720.
33. Zhao, Y.; Zhang, P.; Yang, Z.; et al. Mechanistic analysis of multiple processes controlling solar-driven H_2O_2 synthesis using engineered polymeric carbon nitride. *Nat. Commun*. **2021**, *12*, 3701.
34. Pels, J.R.; Kapteijn, F.; Moulijn, J.A.; et al. E Evolution of nitrogen functionalities in carbonaceous materials during pyrolysis. *Carbon.* **1995**, *33*, 1641–1653.
35. Wu, Z.L.; Huang, B.K.; Wang, X.H.; et al. Facilely Tuning the First-Shell Coordination Microenvironment in Iron Single-Atom for Fenton-like Chemistry toward Highly Efficient Wastewater Purification. *Environ. Sci. Technol.* **2023**, *57*, 14046–14057.
36. Xiong, Y.; Li, H.C.; Liu, C.W.; et al. Single-atom Fe catalysts for Fenton-like reactions: Roles of different N species. *Adv. Mater.* **2022**, *34*, 2110653.
37. Cui, J.; Shao, S.; Gao, J.; et al. Efficient single-atom Fe-catalyzed Fenton-like reaction involving peroxymonosulfate for BPA degradation by high-valent Fe^{IV}=O. *ACS EST Water.* **2022**, *2*, 2698–2705.
38. Wang, X.R.; Liu, J.Y.; Liu, Z.W.; et al. Identifying the key role of pyridinic-N-Co bonding in synergistic electrocatalysis for reversible ORR/OER. *Adv. Mater.* **2018**, *30*, 1800005.
39. Zhang, P.; Chen, H.C.; Zhu, H.Y.; et al. Inter-site structural heterogeneity induction of single atom Fe catalysts for robust oxygen reduction. *Nat. Commun.* **2024**, *15*, 2062.
40. Lin, Y.F.; Wang, Y.; Weng, Z.L.; et al. Coordination engineering of heterogeneous high-valent Fe(IV)-oxo for safe removal of pollutants via powerful Fenton-like reactions. *Nat. Commun.* **2024**, *15*, 2808.
41. Byrne, T.M.; Gu, X.; Hou, P.; et al. Quaternary nitrogen activated carbons for removal of perchlorate with electrochemical regeneration. *Carbon* **2014**, *73*, 1–12.
42. Qu, S.; Yuan, Y.; Yang, X.; et al. Carbon defects in biochar facilitated nitrogen doping: The significant role of pyridinic nitrogen in peroxymonosulfate activation and ciprofloxacin degradation. *Chem. Eng. J.* **2022**, *441*, 135864.
43. Li, F.; Wan, Z.; Zheng, D.; et al. Self-dispersed Fe single-atom anchored biochar derived from hyperaccumulator residues with intrinsic Zn and Fe for selective peroxymonosulfate activation via electron transfer process. *Chem. Eng. J.* **2024**, *482*, 149052.
44. Liu, T.; Zhang, F.; Ruan, L.; et al. Facile synthesis and characterization of crystalline iron phthalocyanine. *Mater. Lett.* **2019**, *237*, 319–322.
45. Wang, J.; Huang, Z.Q.; Liu, W.; et al. Design of N-coordinated dual-metal sites: A stable and active Pt-free catalyst for acidic oxygen reduction reaction. *J. Am. Chem. Soc.* **2017**, *139*, 17281–17284.
46. Zeng, T.; Tang, X.; Huang, Z.; et al. Atomically dispersed Fe–N_4 site as a conductive bridge enables efficient and stable activation of peroxymonosulfate: Active site renewal, anti-oxidative capacity, and pathway alternation mechanism. *Environ. Sci. Technol.* **2023**, *57*, 20929–20940.
47. Jiang, X.; Li, C.; Chen, Y.; et al. Universal scalable production of single-atom catalysts for antibiotic wastewater treatment. *Nat. Water.* **2026**, *4*, 206–216.

48. Chen, T.; Zhang, G.; Sun, H.; et al. Robust Fe-N_4-C_6O_2 single atom sites for efficient PMS activation and enhanced Fe^{IV} = O reactivity. *Nat. Commun.* **2025**, *16*, 2402.
49. Wang, F.; Fan, Y.; Kong, D.; et al. Sequestration and degradation of waterborne pollutants in N-doped porous carbon decorated with Fe single sites. *Environ. Sci. Technol.* **2025**, *5*, 1525–1537.
50. Fan, Y.; Chu, M.; Li, H.; et al. Optimal oxophilicity at the Fe-N_x interface enhances the generation of singlet oxygen for efficient Fenton-like catalysis. *Small* **2024**, *20*, 202403804.
51. Zeng, Y.; Deng, J.; Zhou, N.; et al. Mediated Peroxymonosulfate Activation at the Single Atom Fe-N_3O_1 Sites: Synergistic Degradation of Antibiotics by Two Non-Radical Pathways. *Small* **2024**, *20*. 202311552.
52. Zeng, Y.; Almatrafi, E.; Xia, W.; et al. Nitrogen-doped carbon-based single-atom Fe catalysts: Synthesis, properties, and applications in advanced oxidation processes. *Coord. Chem. Rev*. **2023**, *475*, 214874.
53. Luo, J.M.; Bo, S.F.; Qin, Y.N.; et al. Transforming goat manure into surface-loaded cobalt/biochar as PMS activator for highly efficient ciprofloxacin degradation. *Chem. Eng. J.* **2020**, *395*, 125063.
54. Deng, J.; Xu, M.Y.; Feng, S.F.; et al. Iron-doped ordered mesoporous Co_3O_4 activation of peroxymonosulfate for ciprofloxacin degradation: Performance, mechanism and degradation pathway. *Sci. Total Environ.* **2019**, *658*, 343–356.
55. Ma, J.; Graham, N.J.D. Degradation of atrazine by manganese-catalysed ozonation-Influence of radical scavengers. *Water Res.* **2000**, *34*, 3822–3828.
56. Wang, L.; Xu, H.; Jiang, N.; et al. Trace cupric species triggered decomposition of peroxymonosulfate and degradation of organic pollutants: Cu(III) being the primary and selective intermediate oxidant. *Environ. Sci. Technol.* **2020**, *54*, 4686–4694.
57. Guo, S.; Gao, X.; Huang, Y.; et al. Efficient Degradation of Ciprofloxacin via Peroxymonosulfate Activation over a Hierarchically Porous Cu–Ti Alloy Manufactured by 3D Printing. *ACS EST Water* **2024**, *5*, 33–41.
58. Yun, E.T.; Lee, J.H.; Kim, J.; et al. Identifying the Nonradical Mechanism in the Peroxymonosulfate Activation Process: Singlet Oxygenation Versus Mediated Electron Transfer. *Environ. Sci. Technol*. **2018**, *52*, 7032–7042.
59. Yang, L.; Chen, Y.; Ouyang, D.; et al. Mechanistic insights into adsorptive and oxidative removal of monochlorobenzene in biochar-supported nanoscale zero-valent iron/persulfate system. *Chem. Eng. J.* **2020**, *400*, 125811.
60. Zhang, M.; Luo, R.; Wang, C.; et al. Confined pyrolysis of metal–organic frameworks to N-doped hierarchical carbon for non-radical dominated advanced oxidation processes. *J. Mater. Chem. A* **2019**, *7*, 12547–12555.
61. Chen, F.; Liu, L.L.; Wu, J.H.; et al. Single-Atom Iron Anchored Tubular g-C3N4 Catalysts for Ultrafast Fenton-Like Reaction: Roles of High-Valency Iron-Oxo Species and Organic Radicals. *Adv. Mater*. **2022**, *34*, 202202891.
62. Liu, X.R.; Qin, H.H.; Xing, S.Y.; et al. Selective removal of organic pollutants in groundwater and surface water by persulfate-assisted advanced oxidation: The role of electron-donating capacity. *Environ. Sci. Technol.* **2023**, *57*, 13710–13720.
63. Cui, J.; Li, L.; Shao, S.; et al. Regulating the metal–support interaction: Double jump to reach the efficiency apex of the Fe–N_4-catalyzed Fenton-like reaction. *ACS Catal.* **2022**, *12*, 14954–14963.
64. Li, J.; Xia, W.; Tang, J.; et al. Metal–organic framework-derived graphene mesh: A robust scaffold for highly exposed Fe–N_4 active sites toward an excellent oxygen reduction catalyst in acid media. *J. Am. Chem. Soc.* **2022**, *144*, 9280–9291.
65. Wang, Q.; Zhou, Z.-Y.; Lai, Y.-J.; et al. Phenylenediamine-based FeN_x/C catalyst with high activity for oxygen reduction in acid medium and its active-site probing. *J. Am. Chem. Soc.* **2014**, *136*, 10882–10885.
66. Mun, Y.; Lee, S.; Kim, K.; et al. Versatile strategy for tuning ORR activity of a single Fe-N_4 site by controlling electron-withdrawing/donating properties of a carbon plane. *J. Am. Chem. Soc.* **2019**, *141*, 6254–6262.
67. Wang, Z.; Wang, W.; Wang, J.; et al. High-valent iron-oxo species mediated cyclic oxidation through single-atom Fe-N_6 sites with high peroxymonosulfate utilization rate. *Appl. Catal. B* **2022**, *305*, 121049.
68. Zong, Y.; Guan, X.; Xu, J.; et al. Unraveling the overlooked involvement of high-valent cobalt-oxo species generated from the cobalt(II)-activated peroxymonosulfate process. *Environ. Sci. Technol.* **2020**, *54*, 16231–16239.
69. Cui, J.; Li, L.; Wu, Y.; et al. Robust Fe-N_4 center with optimized metal-support interaction for efficient pollutant degradation by Fenton-like reaction. *Appl. Catal. B* **2023**, *331*, 122706.
70. Bao, Y.; Lian, C.; Huang, K.; et al. Generating high-valent iron-oxo≡Fe^{IV}=O complexes in neutral microenvironments through peroxymonosulfate activation by Zn–Fe layered double hydroxides. *Angew. Chem. Int. Ed.* **2022**, *61*, 202209542.
71. Wu, X.L.; Liu, S.; Li, Y.; et al. Directional and Ultrafast Charge Transfer in Oxygen-Vacancy-Rich ZnO@Single-Atom Cobalt Core-Shell Junction for Photo-Fenton-Like Reaction. *Angew. Chem. Int. Ed.* **2023**, *62*, 202305639.
72. Cheng, C.; Ren, W.; Miao, F.; et al. Generation of Fe^{IV}=O and its Contribution to Fenton-Like Reactions on a Single-Atom Iron–N–C Catalyst. *Angew. Chem. Int. Ed.* **2023**, *62*, 202218510.
73. Mi, X.; Wang, P.; Xu, S.; et al. Almost 100 % Peroxymonosulfate Conversion to Singlet Oxygen on Single-Atom CoN_{2+2} Sites. *Angew. Chem. Int. Ed.* **2021**, *60*, 4588–4593.
74. Deng, Y.; Zhou, Y.; Song, Z.; et al. Long-Range Electronically Polarized Fe-N_5 Catalysts Redirect Polymerization-Driven Phenolic Pollutant Removal Toward Sustainable Carbon Sequestration. *Angew. Chem. Int. Ed.* **2025**, *64*, 202509493.
75. Ye, F.; Wang, J.-R.; Ding, Y.; et al. Photoswitching-Modulated Interfacial Electron Transfer in Single-Atom Co-

TiO2 for Enhanced Pollutant Mineralization in Persulfate-Based AOPs. *Environ. Sci. Technol.* **2025**, *59*, 17869–17880

76. Huang, B.; Ren, X.; Zhao, J.; et al. Modulating Electronic Structure Engineering of Atomically Dispersed Cobalt Catalyst in Fenton-like Reaction for Efficient Degradation of Organic Pollutants. *Environ. Sci. Technol.* **2023**, *57*, 14071–14081.
77. Zhu, K.; Wang, L.; Hu, Z.; et al. Curved interface-induced Jahn-Teller effect in single-atom catalysts for water purification. *Nat. Commun.* **2025**, *16*, 11047.
78. Li, S.; Wang, W.; Wu, H.; et al. Facile cascade-anchored synthesis of ultrahigh metal loading single-atom for significantly improved Fenton-like catalysis. *Nat. Commun.* **2025**, *16*, 8796.